Muskie: Multi-view Masked Image Modeling for 3D Vision Pre-training

Wenyu Li[†] Sidun Liu[†] Peng Qiao* Yong Dou* Tongrui Hu

National University of Defense Technology

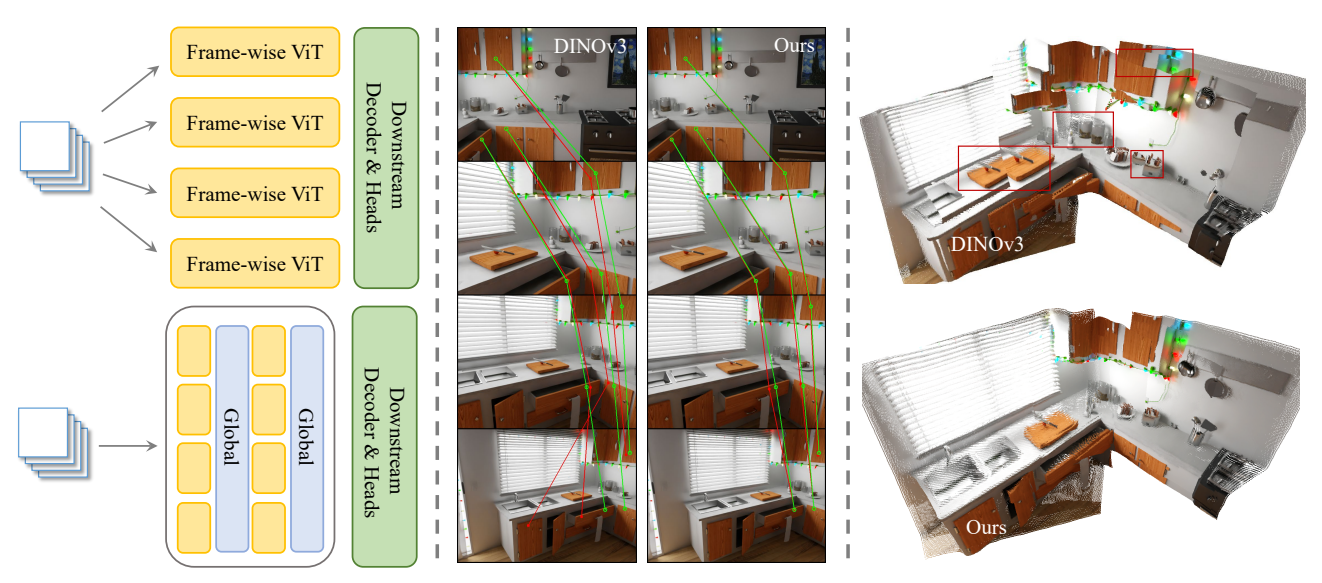


Figure 1. **Muskie** is a native multi-view visual backbone designed for 3D vision tasks. Through Multi-view Masked Image Modeling pre-training, it learns to jointly extract representations across multiple views in a single forward pass. This is in contrast to the conventional frame-wise paradigm, where a ViT independently encodes each view before features are fused. Muskie establishes stronger multi-view consistency, demonstrated by predicted tracks (red) that align closely with the ground truth (green). Using Muskie as a backbone also leads to superior performance in applications like pointmap estimation, where it produces coherent and geometrically complete 3D reconstructions.

Abstract

We present Muskie, a native multi-view vision backbone designed for 3D vision tasks. Unlike existing models, which are frame-wise and exhibit limited multi-view consistency, Muskie is designed to process multiple views simultaneously and introduce multi-view consistency in pre-training stage. Muskie is trained to reconstruct heavily masked content in one view by finding and utilizing geometric correspondences from other views. Through this pretext task and our proposed aggressive masking strategy, the model implicitly to learn view-invariant features and develop strong geometric understanding without any 3D supervision. Compared with state-of-the-art frame-wise backbones such as DINO, Muskie achieves higher multi-view correspondence accuracy. Furthermore, we demonstrate that using Muskie as a backbone consistently enhances performance on down-

stream 3D tasks, including camera pose estimation and pointmap reconstruction. Codes are publicly available at https://leo-frank.github.io/Muskie/.

1. Introduction

Reconstructing and understanding the 3D world from 2D images is one of the long-standing and fundamental goals in computer vision [28, 29, 37, 38]. A prevailing practice in this domain is to leverage Vision Foundation Models (VFMs), such as the DINO series [23, 32], as powerful feature extractors for downstream 3D tasks like 3D reconstruction and camera pose estimation. These VFMs, pretrained on massive-scale 2D image datasets, have achieved remarkable success and become the de-facto backbones for many modern approaches [9, 17, 40, 44, 55].

However, recent studies [11, 15] revealed that existing

[†]Equal Contribution *Corresponding Author

VFMs exhibit limited 3D understanding, notably a lack of *multi-view consistency*, which requires the feature representations to be consistent across different viewpoints, as shown in Fig. 1. This capability is a core requirement for 3D tasks as it enables the accurate aggregation of information across views. While prior efforts have sought to instill 3D awareness into VFMs by leveraging supervisory signals from depth maps [15] or camera poses [41], their reliance on 3D annotations limits scalability and generalizability.

We posit that the key to achieving robust multi-view consistency lies in addressing it directly during the self-supervised pre-training phase. This insight stems from a core limitation in existing VFMs: their frame-wise pre-training paradigm. This paradigm operates only on single-view images, providing no incentive for the model to learn cross-view relationships. Consequently, when these models are applied to multi-view settings, they process each image independently and fail to establish consistency.

To this end, we propose Muskie to instill multi-view consistency during pre-training by introducing the multi-view completion task, which extends Masked Image Modeling (MIM)[14, 47] to the multi-view domain. Given multi-view observations as input, the core idea of this pretext task is to reconstruct masked regions in one view by leveraging the visible content from other available views. This pretext task implicitly compels the model to discover geometric correspondences, resulting in view-consistent features without explicit 3D annotations.

To make the pre-training scheme effective, we first need to prevent the model from taking shortcuts—that is, reconstructing masked regions using only intra-view cues like conventional MIM methods. We address this by proposing an aggressive masking strategy with high masking ratios and spatially concentrated mask blocks. By masking large and contiguous blocks, this method makes single-view reconstruction nearly impossible, thus compelling the model to seek correspondences across views. Furthermore, to process multi-view inputs, we incorporate Alternating Attention[40], which facilitates efficient information exchange both intra-view and inter-view.

We pre-train Muskie on large-scale, unlabeled multiview image collections. The trained model demonstrates superior multi-view correspondence accuracy over state-of-the-art visual backbones, such as DINO family[23, 32] and MAE[14]. We further evaluate it as a backbone within end-to-end 3D reconstruction frameworks [44] for pointmap and camera pose estimation, observing consistent improvements across these downstream tasks. The results show that our multi-view pre-training effectively builds geometric understanding into visual features, enabling 3D-aware representations. In summary, our contributions are three-fold:

• We introduce Muskie, a novel pre-training framework that learns 3D-aware representations from multi-view im-

- ages without any 3D supervision.
- We show that Muskie produces superior geometric consistency, demonstrating that our pre-training effectively equips the model with geometric reasoning capability.
- We demonstrate that using Muskie as a feature extractor enhances the performance of downstream 3D tasks, outperforming state-of-the-art backbones that are restricted to single-image pre-training.

2. Related Works

Self-supervised learning from 2D images. The rise of Vision Foundation Models (VFMs), trained via selfsupervised learning on vast 2D image datasets without annotations, has marked a paradigm shift in computer vision. These models learn powerful general-purpose representations typically through one of two dominant approaches: contrastive learning [6, 7, 12, 13, 23, 32], which learns by leveraging discriminative signals between images, or masked image modeling [14, 36, 47], inspired by the masked token prediction task in BERT[10]. Both approaches excel at learning robust dense features, such as semantic object boundaries, leading to high performance on downstream tasks such as segmentation[1, 20] and depth estimation[42, 49, 50]. However, these methods are trained exclusively on unstructured 2D image collections, thus lacking knowledge of the underlying 3D structure.

Incorporating 3D Awareness into VFMs. To enhance the 3D understanding of VFMs, a key research direction is to instill geometric awareness during self-supervised pre-training. Early approaches focused on incorporating explicit 3D priors into contrastive learning frameworks. For instance, Pri3D[15] enforced multiview consistency using geometric correlations from RGB-D scans, while other works leveraged publicly available CAD models[3] or known relative camera poses[41]. However, the reliance on such annotated 3D data limit the scalability and performance gains. A more recent line of work, CroCo[45, 46], adapts the masked image modeling strategy to stereo data to learn 3D priors. However, this approach is limited by its pair-wise input structure, which constrains its applicability to stereo-only tasks.

Feed-Forward 3D Reconstruction Models. Recent learning-based approaches have shifted toward end-to-end frameworks that predict 3D structure from multi-view unposed images within a single pass[9, 17, 40, 43, 44, 48, 55]. Among these works, VGGT[40] first scales the model to a 1.2B parameter transformer that jointly predicts intrinsics, extrinsics and pointmaps. π^3 [44] furthermore finds that the reliance on a fixed reference view can lead to failures if the reference is suboptimal and propose to predict local pointmaps without any reference frames. These modern approaches leverage the DINOv2[23] as image encoder

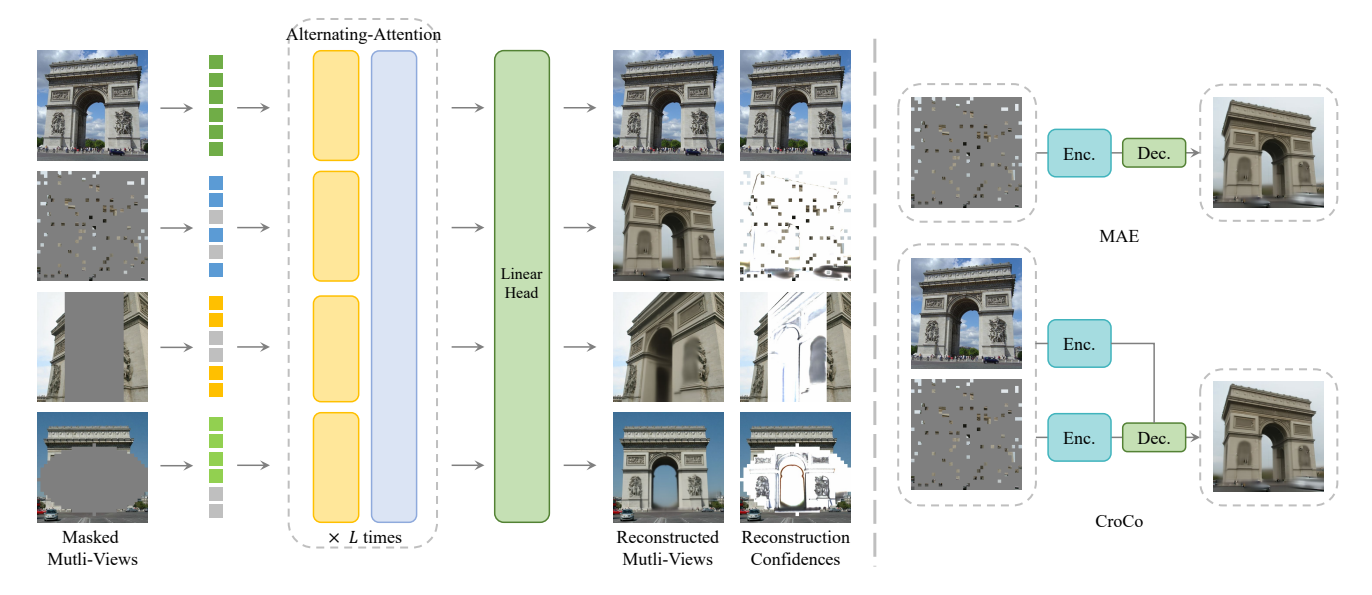


Figure 2. **Overview of Muskie architecture.** Multi-view images are divided into patches, and a portion of them is masked using various masking shapes (random, rectangular, or elliptical), replaced with learnable tokens. A subset of views is kept unmasked to serve as reference for others. These patches are jointly processed via stacked alternating-attention blocks[40]. A lightweight linear head reconstructs the masked patches along with confidence maps. For comparison, MAE[14] performs Masked Image Modeling (MIM) in a single-view setting, while CroCo[45, 46] extends MIM to dual views but still encodes each view independently during the encoding stage.

due to its curated pre-training and powerful emergent properties. However, we demonstrate that the frame-wise processing leads to poor consistency and is suboptimal for 3D tasks.

3. Method

In this section, we present Muskie, a self-supervised pretraining framework designed to learn 3D-aware visual representations. The core principle of Muskie is to train a model to solve a challenging multi-view completion task. By learning to reconstruct heavily masked content in one view using information from other views, the model is implicitly forced to find geometric correspondences and develop view-invariant features. We detail the design of pretext task, model architecture, and training objective below.

3.1. Pretext Task

At the core of our method is a pretext task designed to solve a challenging multi-view completion task. Formally, let $\mathcal{X} = \{x_1, x_2, \dots, x_V\}$ be a collection of V images of the same scene captured from different viewpoints. Each image $x_i \in \mathcal{X}$ is first divided into a sequence of N non-overlapping patches, denoted as $\{p_{i,j}\}_{j=1}^N$. For each view i, we randomly mask a large portion of its patches. Let \mathcal{M} be the set of indices (i,j) corresponding to all masked patches across all views, with $r \in [0,1]$ being a masking ratio hyperparameter. The objective of our pretext task is to reconstruct the original pixel values of all masked patches $\{p_{i,j}|(i,j)\in \mathcal{M}\}$ by observing the remaining visi-

ble patches from all views, as shown in Fig. 2.

This formulation marks a fundamental departure from conventional single-view Masked Image Modeling (MIM). While single-view MIM encourages the learning of semantic and textural regularities within a single image (e.g., reconstructing a cat's ear from its face), it primarily relies on contextual reasoning. In our setting, however, we make reconstruction from single-view context nearly impossible by masking large, contiguous regions. This design compels the model to shift from contextual reasoning to geometric reasoning. To reconstruct a heavily masked patch in view B, it must identify and utilize the corresponding patch from another view A. In essence, the model is implicitly forced to answer the question: What patch in view A corresponds to this masked patch in view B? This shift is the cornerstone of Muskie's ability to learn 3D-aware representations without requiring any explicit 3D supervision.

3.2. Model Design

Architecture Design. To jointly process patch tokens from multiple views, we adopt stacked Alternating Attention (AA) blocks following the design of VGGT [40]. Each block alternates between frame-wise and global attention, enabling hierarchical aggregation of intra- and inter-view information. In particular, the global attention operates across views through cross-view query-key interactions, effectively associating spatially corresponding regions between different viewpoints. This mechanism implicitly establishes correspondences, thereby encouraging the emer-

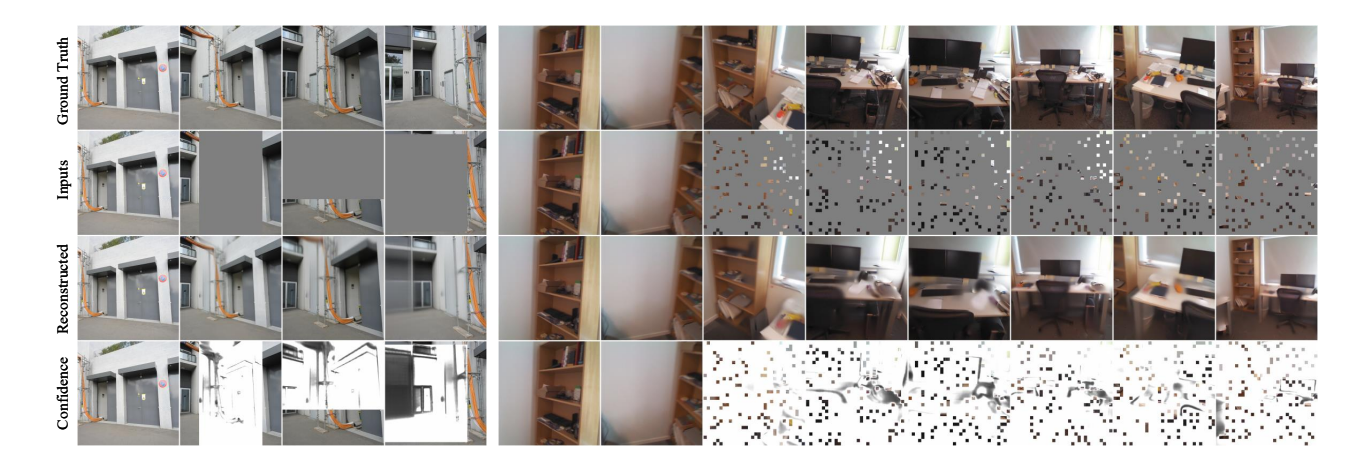


Figure 3. Visualizations of the reconstructions from masked images. Samples are taken from ETH3D[30] and 7Scenes[31]. Left: The model successfully reconstructs co-visible regions. Meanwhile, for areas that are not co-visible (e.g., newly exposed surfaces due to camera motion), the model produces a blurry reconstruction and assigns a low confidence score. Right: In a more challenging scenario where the reference views provide little information, the model can aggregate information from sparse cues to reconstruct.

gence of multi-view consistent feature representations. Unlike VGGT [40], which distinguishes between primary and secondary views, Muskie treats all views equally and ensures permutation equivariance. We further incorporate Rotary Positional Embeddings (RoPE) [33] to enhance resolution adaptability. A lightweight linear head is used to decode pixel values and confidence maps during pre-training and is discarded afterwards.

Masking Strategy. The design of our masking strategy is driven by a primary objective: to eliminate shortcuts. We define a shortcut as any mechanism by which the model can reconstruct masked content using only information from a single view, thereby bypassing the need to learn multi-view geometric correspondences. We introduce three key principles to achieve this. First, we employ a high masking ratio. A low ratio would create an obvious shortcut: the model could simply rely on the rich local context within a single frame for reconstruction. Our masking ratio is considerably higher than the 75% used in MAE[14]. Second, besides random masks with high ratio, we apply spatially concentrated masks (e.g., large contiguous blocks) instead of random perpatch masking only. This design prevents the model from leveraging sparse structure cues that can persist in a single, randomly masked view. By masking large, contiguous regions, we make single-view reconstruction nearly impossible, forcing the model to seek information from other views. Specifically, we apply rectangular and elliptical region masks as shown in Fig. 2. Thirdly, a subset of views remain unmasked to serve as reference. The ablation study in Tab. 6 validates these three principles.

3.3. Training

Objective Function. The training objective is to minimize the reconstruction error in the pixel space for the masked patches. Since certain masked regions may not contain adequate contextual information for reliable reconstruction, we adopt a confidence-aware \mathcal{L}_2 loss to adaptively weight the reconstruction objective. In addition to stabilizing training, the learned confidence maps implicitly encode cross-view correspondence cues, which further benefit multi-view understanding. For each patch in the masked set \mathcal{M} , the model outputs both the reconstructed pixel values $\hat{p}_{i,j}$ and a corresponding confidence score $c_{i,j}$, which is normalized to [0,1] by a sigmoid function. The confidence-aware \mathcal{L}_2 loss is formally defined as:

$$\mathcal{L} = \frac{1}{|\mathcal{M}|} \sum_{(i,j) \in \mathcal{M}} \left[(c_{i,j} + \epsilon) \|\hat{p}_{i,j} - p_{i,j}\|_2^2 - \lambda \log c_{i,j} \right],$$
(1)

where ϵ and λ are set to 0.1 in all experiments.

Training Data. We pre-train Muskie on a large-scale and diverse collection of multi-view datasets, comprising a mixture of: Co3Dv2 [25], BlendedMVG [51], ARkitScenes [5], DL3DV [22], MegaDepth [21], ScanNet++ [52], Hyper-Sim [26], Waymo [34] and RealEstate10K[54]. This curated collection spans a wide range of domains—from indoor and outdoor scenes to synthetic and real-world captures—ensuring the model learns generalizable features. In total, our pre-training dataset is comparable in scale and diversity to that used by recent feed-forward 3D Reconstruction models such as VGGT[40].

Implementation Details. During pre-training, the model is trained with mixed image resolutions and aspect ratios, including 224, 384, and 512 pixels. The number of input

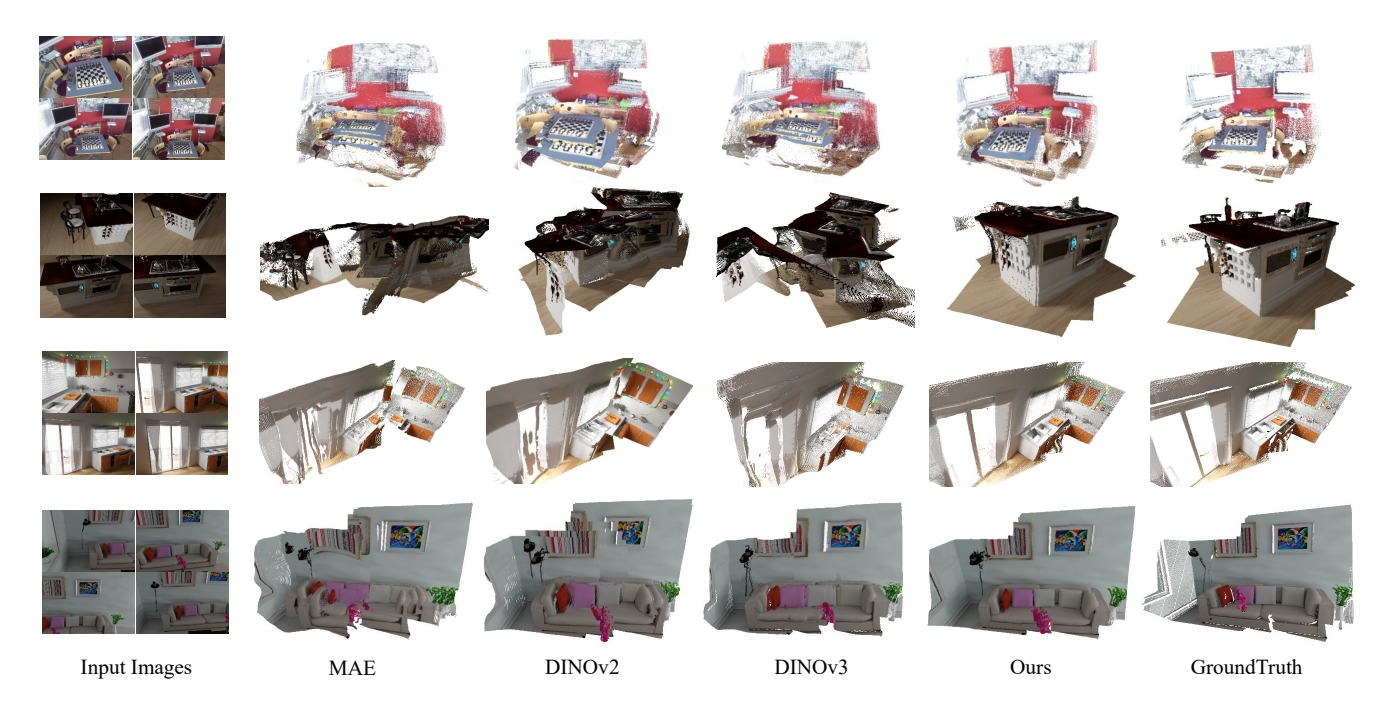


Figure 4. Qualitative comparison of predicted pointmaps for 7Scenes[31] and NRGBD[4]. We compare the 3D reconstruction results of our method against baselines using different visual backbones. Our method consistently produces reconstructions that more complete and more faithful to the ground truth geometry across all scenes.

views is randomly varied between 2 and 8 for each training sample to enhance robustness across different multiview configurations. We adopt the AdamW[18] optimizer with a learning rate of 2×10^{-4} , following a cosine decay schedule and a 2-epoch warm-up. The pre-training runs for 400 epochs with 200K randomly sampled image groups per epoch. For each image group, we select adjacent views based on image IDs to improve sample effectiveness. Standard data augmentations, including random cropping and flipping, are applied to improve generalization. We train two model sizes, Muskie-B and Muskie-L, with parameter counts equal to the standard ViT-Base and ViT-Large, respectively. The training runs on 8 A100 GPUs about two weeks for Muskie-L and one week for Muskie-B. We provide visualization of two challenging scenes unseen during pre-training, which shows strong evidence that the model has learned to solve the multi-view completion task.

4. Experiments

We evaluate Muskie pre-training through a threefold analysis. First, we analyze the geometric consistency of its learned features. Second, we assess its performance as the backbone for downstream 3D geometric tasks against state-of-the-art methods. Finally, we conduct ablation studies to investigate the impact of our key design choices.

4.1. Zero-Shot Correspondence Quality

The core idea of Muskie is to learn geometrically consistent features. We validate this directly by evaluating the model's zero-shot correspondence quality, isolating the effect of our pre-training from any downstream fine-tuning.

Implementations. Our evaluation is performed on multiview image sequences, each consisting of 8 frames. For each sequence, we sample a set of points in the first frame and track their corresponding 2D locations in all subsequent frames. The performance is then measured by the error between the predicted tracks and the ground-truth tracks. A key difference in this evaluation lies in how correspondences are extracted from our native multi-view model versus the frame-wise baselines. For Muskie, we perform a single forward pass over all views and extract attention maps from global attention layer, from which a dense correlation volume is regressed using a soft-argmax operation to extract correspondence. For baseline frame-wise models, we extract dense features for each view. Correspondences are then established via nearest-neighbor matching in the feature space.

Datasets and Metrics. Following the setup in [11], we evaluate on both indoor scenes from Paired ScanNet split[8, 27]* and objects from NAVI[16]. We report performance

^{*}The ScanNet splits used for evaluation have no overlap with the ScanNet++ data used during our pre-training.

Dataset	Method		$R@k\uparrow$			$T@k\uparrow$		P	AUC@k	↑	Po	intmap l	Estimatio	n↓
Dutuset	Wellou	@5	@15	@30	@5	@15	@30	@5	@15	@30	Acc	Comp	Overall	$ \mathcal{L}_1 $
	MAE-L[14]	22.571	50.071	62.786	0.857	6.357	20.000	0.029	1.081	4.536	0.055	0.107	0.081	0.129
	DINOv2-L[23]	49.143	81.071	91.000	0.714	7.929	23.357	0.186	2.181	8.514	0.039	0.042	0.041	0.074
70	DINOv3-L[32]	38.929	65.500	72.214	1.929	10.357	25.786	0.314	3.729	9.826	0.050	0.092	0.071	0.115
7Scenes	Muskie-B	74.214	97.357	98.786	5.857	32.857	60.071	1.414	13.810	31.231	0.039	0.041	0.040	0.051
	Muskie-L	90.143	99.214	100.000	16.286	52.143	78.571	6.100	26.929	47.345	0.025	0.028	0.027	0.035
	π^{3} (ref.)[44]	94.571	100.000	100.000	37.643	74.214	86.857	16.200	46.029	64.069	0.014	0.016	0.015	0.022
	MAE-L[14]	40.286	62.143	75.786	2.571	15.071	36.643	0.400	4.276	12.781	0.073	0.116	0.095	0.129
	DINOv2-L[23]	60.500	82.143	87.714	5.071	30.500	56.643	1.057	10.238	25.986	0.060	0.089	0.075	0.096
NRGBD	DINOv3-L[32]	45.714	73.000	77.857	4.500	18.357	41.143	0.857	6.229	16.195	0.064	0.101	0.083	0.114
NKGBD	Muskie-B	70.643	88.357	89.643	13.571	53.571	77.000	3.686	25.038	<u>45.433</u>	0.058	0.090	0.074	0.090
	Muskie-L	92.714	94.143	94.214	41.571	80.071	89.857	19.457	50.957	67.452	0.046	0.077	0.061	0.067
	π^{3} (ref.)[44]	94.714	95.071	95.143	79.286	92.071	96.000	57.800	77.495	84.843	0.031	0.060	0.046	0.044

Table 1. Quantitative results on 7Scenes[31] and NRGBD[4] datasets for 3D reconstruction. These two dataset are not trained in pre-training and downstream finetuning. Best results are in bold.

Method	Pixe	el Space	(px)	3D S	Space (cr	n)
	ATE ↓	@5↑	@10↑	ATE ↓	@2↑	@5↑
CLIP[24]	189.22	12.97	13.35	13.86	23.84	41.10
SigLIP[53]	111.66	13.66	15.71	7.79	43.46	68.41
SAM[19]	69.54	15.68	22.28	4.56	62.58	81.66
DIFT[35]	60.44	16.97	26.46	4.93	64.36	81.21
MAE[14]	81.24	14.63	19.11	5.25	54.73	78.19
CroCov2[46]	56.79	19.77	32.58	4.42	72.15	84.66
DINOv2[23]	53.31	16.94	26.29	4.24	69.97	84.23
DINOv3[32]	41.15	17.23	27.95	3.76	74.89	87.11
Muskie-B	42.54	19.48	31.95	2.93	75.90	89.17
Muskie-L	29.42	22.29	39.21	2.38	82.74	91.87

Table 2. Quantitative results on the NAVI[16] dataset for zero-shot correspondence.

Method	Pixe	el Space	(px)	3D S	Space (cn	n)
Wichiod	ATE ↓	@5↑	@10↑	ATE↓	@2↑	@5↑
CLIP[24]	203.18	20.83	21.04	102.45	22.47	22.95
SigLIP[53]	142.96	21.04	21.78	81.44	23.04	24.88
SAM[19]	76.12	23.80	31.16	49.85	27.34	36.56
MAE[14]	104.94	22.07	25.18	62.70	24.01	28.51
CroCov2[46]	25.92	34.20	55.93	29.84	38.16	58.02
DINOv2[23]	72.11	23.42	29.22	49.09	27.13	34.29
DINOv3[32]	55.78	24.66	33.54	42.58	29.49	41.69
Muskie-B	33.77	31.41	47.67	31.67	35.03	51.14
Muskie-L	24.68	<u>33.83</u>	<u>52.96</u>	27.82	<u>37.52</u>	<u>56.60</u>

Table 3. Quantitative results on the ScanNet[8] dataset for zero-shot correspondence.

using two primary metrics: (1) 2D pixel error, which includes the Average Trajectory Error (ATE) in pixels and ac-

curacy at various pixel thresholds (Acc@k px); and (2) 3D metric error, where we unproject points into 3D space to compute ATE in centimeters and accuracy at various centimeter thresholds (Acc@k cm). We only consider points that are visible in the ground truth for a fair evaluation.

Results. The quantitative results, presented in Tabs. 2 and 3, highlight the superior multi-view consistency of our Muskie models across both objects and scenes.† On the object-centric NAVI[16] dataset, Muskie-L achieves a remarkable 3D-space ATE of just 2.38 cm, a 36% error reduction over the DINOv3. Our model's performance advantage is also pronounced on the ScanNet[8] dataset, where the smaller Muskie-B model outperforms all frame-wise baselines. CroCo[46] performs well on ScanNet[8] but generalizes poorly to object-centric NAVI[16] due to its indoorfocused training data. In contrast, our models show consistent gains across both datasets, demonstrating stronger geometric generalization. Meanwhile, we present a qualitative comparison of predicted correspondences in Fig. 5. We visualize the predicted tracks in red and the ground-truth tracks in green. The close alignment between the red and green paths highlights Muskie's ability to maintain highquality correspondence even in texture-less areas.

4.2. Performance on 3D Reconstruction Tasks

In this section, we evaluate Muskie's utility as a generalpurpose backbone for 3D vision. We replace the standard encoder in a state-of-the-art 3D reconstruction framework with ours and measure the resulting performance gains.

[†]All baseline VFMs are in their Large variants, except for CroCov2 which uses a Large encoder and a Base decoder.



Figure 5. Qualitative comparison of multi-view correspondence estimation. Sequences are sampled from the NAVI[16], ScanNet[8], and NRGBD[4]. We visualize the predicted tracks (red) and the ground-truth tracks (green). Points are only rendered in frames where the GT point is visible. The close alignment between the red and green paths highlights our method's ability to maintain accurate consistency.

Implementations. We evaluate Muskie by integrating it as the feature backbone of the state-of-the-art π^3 [44] reconstruction pipeline, which offers permutation equivariance and faster convergence than VGGT [40]. To better isolate the encoder's contribution, we simplify 36-layer decoder of π^3 to a lightweight 4-layer version. For all experiments, we replace the original DINOv2 [23] backbone in this simplified framework with different frame-wise ViTs like MAE[14], DINOv3 [32], and Muskie series, while keeping all other components and hyperparameters identical. This setup enables a fair comparison focused solely on the encoder's impact on reconstruction quality.

Training and Evaluation Protocol. We train all downstream models on ARKitScenes [5], ScanNet++ [52], and BlendedMVS [51], forming a lighter setup than the full corpus used by π^3 [44]. We evaluate performance on the 7Scenes[31] and NeuralRGBD[4] benchmarks. For each scene, we randomly sample 8 frames. The predicted point cloud is aligned to the ground truth using the Umeyama[39] algorithm. For pointmap reconstruction, we report the smallest L2-distance between prediction to ground truth as

Accuracy, the smallest L2-distance from ground truth to prediction as Completeness and their average as Overall. We also report the mean absolute error ($||\mathcal{L}_1||$). Lower values in Acc., Comp., Overall, and $||\mathcal{L}_1||$ indicate better reconstruction quality. For camera pose regression, we measure rotation and translation accuracy (R@K and T@K) at thresholds K=5,15,30, together with the area under the accuracy curve (AUC@K).

Results. The quantitative results are shown in Tab. 1. In both pointmap reconstruction and camera pose estimation, Muskie-powered models consistently outperform all other baselines. For instance, on the 7Scenes[31], Muskie substantially outperforms the widely-adopted DINOv2; it boosts the overall camera pose accuracy (AUC@30) from 8.514 to a remarkable 47.345, and reduces the pointmap $||\mathcal{L}_1||$ error from 0.074 to 0.035. Notably, the smaller Muskie-B variant consistently surpasses the larger DINOv2-L and DINOv3-L across nearly all metrics. In addition, while π^3 [44] attains strong results with a 36-layer decoder, our Muskie-L with 4-layer decoder achieves highly competitive performance, particularly in

		Camera Pose		Pointmap)	
	AUC@5	AUC@15	AUC@30	Acc	Comp	\mathcal{L}_1
w/o pre-train w pre-train	0.021 2.671	0.598 18.305	3.760 37.413		0.1123 0.0543	

Table 4. **Ablation on the effects of architecture and pretraining.** Metrics are averaged over the 7Scenes [31] and NRGBD [4]. Muskie (w/o pre-train) variant reflects the architectural changes without pre-training benefits, while Muskie (w pre-train) incorporates the full pre-training process.

Input Views	3D@1cm↑	3D@5cm↑	2D@5px↑	2D@25px↑
2	40.59	82.91	4.43	33.74
3	42.89	83.83	4.74	35.50
4	44.45	84.58	5.10	36.80
5	46.13	84.57	5.28	38.38
6	46.75	84.82	5.45	38.91
7	<u>46.97</u>	84.77	5.41	<u>39.26</u>
8	47.36	84.74	<u>5.43</u>	39.52

Table 5. Ablation on the number of context views for correspondence quality on NAVI[16]. We evaluate the correspondence recall between a fixed pair while varying the context number.

Configuration	ATE 2D (px) ↓	Acc@10px ↑	ATE 3D (cm)	Acc@2cm↑
Ablation on Masking Rat	io (Mask Type:	Random, Ref.	Views: 2)	
0.75	22.82	59.50	16.49	36.32
0.80	17.94	61.21	13.97	36.85
0.85	17.28	61.17	13.68	36.67
0.90	16.60	61.33	12.89	36.58
0.95	18.88	55.63	14.43	35.14
Ablation on Mask Type, I	Ref. Views: 2)			
Random (Ratio: 0.90)	16.60	61.33	12.89	36.58
Ours	14.37	63.79	11.83	37.57
Ablation on Number of R	eference Views	(Mask Type: C	Purs)	
0 (No reference)	14.82	63.44	12.55	37.11
1	13.81	65.26	11.27	37.98
2	14.37	63.79	11.83	37.57
4	15.54	63.45	12.68	37.49

Table 6. Ablation on the masking ratio, strategy, and number of reference frames on NRGBD[4]. The results show that our mask strategy with one single reference view yield the best performance.

camera pose estimation. These results strongly suggest that Muskie's pre-training forces the model to learn features that are inherently geometrically consistent, enabling efficient transfer to reconstruct accurate 3D structures. We present a qualitative comparison of estimated pointmaps in Fig. 4, which highlights how our method maintains geometric consistency across views, particularly in challenging areas with repeating or homogeneous textures, such as checkerboards, murals, and sofas.

4.3. Ablation Studies

Pre-training or Architecture. To disentangle the benefits of our architectural design from those of our multi-view pre-training strategy, we conduct an ablation study comparing full, pre-trained Muskie model against an identical archi-



(a) 2 Input Views

(b) 8 Input Views

Figure 6. Impact of multi-view context on correspondence quality from NAVI dataset [16]. We measure matching accuracy on a fixed image pair given (a) only the input pair (2 views) and (b) the pair plus six context views (8 views). Correct matches are shown in green and incorrect matches in red. The additional context yields performance gains, as evidenced by AUC@1cm score.

tecture with randomly initialized weights. The results in Tab. 4, reveal that pre-training is the main factor for performance gain and the architecture-only variant contributes negligibly. This demonstrates that while our architecture provides a capable foundation for multi-view processing, its potential is only fully realized through our self-supervised pre-training.

Effect of Multi-view Context. To verify that Muskie leverages multi-view context for reasoning, we conduct a controlled experiment in Tab. 5. We measure correspondence accuracy on a fixed pair of images while varying the number of additional context views provided to the model. The results show a consistent trend: accuracy on the fixed pair improves as more context views are added. Notably, this performance gain is most pronounced in high-precision metrics like 3D@1cm. This experiment provides strong evidence that Muskie effectively uses information from additional views to refine its correspondence predictions. We present a qualitative comparison in Fig. 6.

Masking Strategy. We conduct an ablation study on the NRGBD[4] to determine the optimal masking strategy. We investigate three key aspects: masking ratio, mask type, and the number of reference views, as shown in Tab. 6. Our mask strategy randomly applies either a rectangular/elliptical mask (75% ratio) or a random per-patch mask (90% ratio) to each training sample. The results show that using our proposed mask strategy with one reference view as final configuration yields the best overall performance.

5. Conclusion

This paper presents Muskie, a multi-view masked image modeling framework for 3D vision pre-training without relying on depth, camera pose, or any other annotations. Our approach trains the model to reconstruct heavily masked

parts of an image using information from other viewpoints and achieves higher geometric correspondences than existing visual backbones. Furthermore, using Muskie as a feature extractor enhances the performance of downstream 3D tasks like 3D reconstruction. This study demonstrates the potential of self-supervised learning for 3D vision. We believe 3D pre-training is promising and hope our work inspires progress in the computer vision community.

Appendix

A. Experiments

A.1. Zero-Shot Correspondence Evaluation

In the main paper, we evaluate the geometric consistency of our model on a zero-shot point tracking task. Here, we provide the formal definitions for the problem and evaluation metrics. We also present more qualitative examples of zero-shot correspondence in Fig. 13.

Formal Definitions. Given an image sequence comprising V views, $\{I_v\}_{v=1}^V$. For each view I_v , we are provided with its corresponding intrinsic matrix $(K_v \in \mathbb{R}^{3\times 3})$, depth map (D_v) , camera Pose: $T_v \in SE(3)$, representing the camerato-world transformation matrix. The evaluation protocol is as follows:

- 1. In the first view I_1 , we sample N starting points, $\{\mathbf{p}_{i,1}\}_{i=1}^N$, within valid depth regions. Here, $\mathbf{p}_{i,1} = (u_{i,1}, v_{i,1})$ denotes the pixel coordinates.
- 2. The model's objective is to predict the corresponding locations of these points in all subsequent views $\{I_v\}_{v=2}^V$. For each starting point $\mathbf{p}_{i,1}$, the model generates a predicted trajectory $\mathcal{T}_i^{\text{pred}} = \{\mathbf{p}_{i,v}^{\text{pred}}\}_{v=1}^V$, where $\mathbf{p}_{i,v}^{\text{pred}} = (\hat{u}_{i,v}, \hat{v}_{i,v})$.
- 3. We leverage the ground-truth depth and pose information to compute the true trajectory for each point, denoted as $\mathcal{T}_i^{\mathrm{gt}} = \{(\mathbf{p}_{i,v}^{\mathrm{gt}}, m_{i,v})\}_{v=1}^V$. Here, $\mathbf{p}_{i,v}^{\mathrm{gt}}$ is the ground-truth 2D correspondence, and $m_{i,v} \in \{0,1\}$ is a visibility mask, where $m_{i,v}=1$ if and only if point i is visible in view v (i.e., within the image bounds and not occluded).

For a fair evaluation, all error metrics are computed exclusively over the set of ground-truth visible points (i.e., points where $m_{i,v}=1$).

Correspondence Extraction Methods. A key distinction in our evaluation lies in how correspondences are extracted by our method versus the baseline models. Baseline models like DINOv2, SAM, and MAE are fundamentally singleimage encoders. To establish correspondences for these models, we first extract dense feature maps for each of the V views independently. Subsequently, correspondences are found via a pairwise feature matching process. Specifically, for each point in the first view, we find its nearest neighbor in the feature space of every other target view. This process is inherently pairwise; the match between view 1 and view v does not leverage information from any other views in the sequence. Muskie is designed with a native multi-view architecture. It processes all V views simultaneously in a single forward pass. Correspondences are directly inferred from the model's internal *cross-view attention maps*[2].

2D Pixel Error. The 2D Pixel Error quantifies the discrepancy between the predicted point and the ground-truth cor-

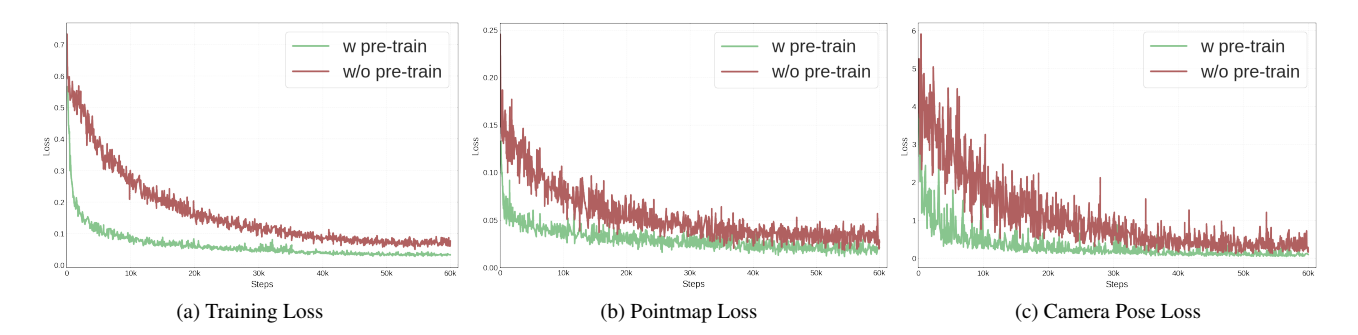


Figure 7. Impact of Pre-training on Convergence Speed and Stability. This figure compares the loss curves when finetuned for 3D reconstruction with pre-trained weights (green) or with random initialization (red). The plots correspond to (a) overall reconstruction loss (b) loss for pointmap estimation and (c) loss for camera pose estimation. The pre-trained model demonstrates faster convergence and reaches a lower, more stable loss, validating the effectiveness of our pre-training strategy presented.

Component	$\pi^{3}[44]$	Baseline	Ours
Encoder	DINOv2-L[23]	Frame-wise backbones	Muskie-L
Decoder	36 layers	4 layers	4 layers
Specialized Heads	5 layers	None	None

Table 7. Comparison of Model Architectures. Our evaluation setup simplifies the original π^3 architecture. Our baseline experiments use various frame-wise ViT backbones (e.g., DINOv2, MAE, SAM). Crucially, all baselines and our method use an identical lightweight 4-layer decoder, which isolates the performance contribution of the encoder.

Method		Number of Input Frames (N)										
	1	4	8	10	20	50	100	200				
DINOv3-B Muskie-B	0.0106 0.0113	0.0105 0.0111	0.0108 0.0114	0.0105 0.0115	0.0129 0.0157	0.0318 0.0392	0.0594 0.0987	0.1153 0.2842				

Table 8. Inference runtime comparison. We measure the inference time (in seconds) across varying numbers of input frames. Both methods utilize PyTorch's optimized scaled dot product attention. Muskie demonstrates superior efficiency in standard lowframe settings ($N \leq 10$) due to a streamlined architecture with lower constant overhead. At higher frame counts, the runtime increases moderately due to the global attention mechanism.

respondence directly in the image space. For any point i that is visible in view v (i.e., $m_{i,v}=1$), its 2D pixel error, $e_{i,v}^{2D}$, is defined as the Euclidean distance between the predicted coordinates $\mathbf{p}_{i,v}^{\text{pred}}$ and the ground-truth coordinates $\mathbf{p}_{i,v}^{\text{gt}}$:

$$e_{i,v}^{2D} = \left\| \mathbf{p}_{i,v}^{\text{pred}} - \mathbf{p}_{i,v}^{\text{gt}} \right\|_{2} \tag{2}$$

Based on this, we define two primary metrics:

• Average Trajectory Error (ATE in pixels): The mean 2D pixel error over all visible tracked points.

$$ATE^{2D} = \frac{\sum_{i=1}^{N} \sum_{v=1}^{V} m_{i,v} \cdot e_{i,v}^{2D}}{\sum_{i=1}^{N} \sum_{v=1}^{V} m_{i,v}}$$
(3)

• Accuracy (Acc@k px): The percentage of visible points for which the 2D pixel error is less than a threshold of k pixels.

$$\text{Acc@k px} = \frac{\sum_{i=1}^{N} \sum_{v=1}^{V} m_{i,v} \cdot \mathbb{I}(e_{i,v}^{2D} < k)}{\sum_{i=1}^{N} \sum_{v=1}^{V} m_{i,v}} \times 100\%$$
(4)

where $\mathbb{I}(\cdot)$ is the indicator function.

3D Metric Error. The 3D Metric Error measures the positional deviation in 3D space that results from the 2D prediction error. We first define an unprojection function $\pi^{-1}(\mathbf{p}, D, K)$, which lifts a 2D point $\mathbf{p} = (u, v)$ from a view into the camera's 3D coordinate system using the depth map D and intrinsics K.

$$\mathbf{P} = \pi^{-1}(\mathbf{p}, D, K) = D(u, v) \cdot K^{-1} \cdot [u, v, 1]^{T}$$
 (5)

where \mathbf{P} is the resulting 3D point coordinate. For any point i visible in view v ($m_{i,v} = 1$), we unproject both its groundtruth 2D coordinates and its predicted 2D coordinates into 3D space. We use the ground-truth depth map D_v for both unprojections. This ensures that we are isolating the 3D error caused by the 2D tracking inaccuracy, rather than evaluating the model's own depth estimation capabilities.

- Ground-Truth 3D Point: $\mathbf{P}_{i,v}^{\mathsf{gt}} = \pi^{-1}(\mathbf{p}_{i,v}^{\mathsf{gt}}, D_v, K_v)$ Predicted 3D Point: $\mathbf{P}_{i,v}^{\mathsf{pred}} = \pi^{-1}(\mathbf{p}_{i,v}^{\mathsf{pred}}, D_v, K_v)$

The 3D metric error for this point, $e_{i,v}^{3D}$, is the Euclidean distance between these two 3D points:

$$e_{i,v}^{3D} = \left\| \mathbf{P}_{i,v}^{\text{pred}} - \mathbf{P}_{i,v}^{\text{gt}} \right\|_{2} \tag{6}$$

This leads to the corresponding 3D metrics:

• Average Trajectory Error (ATE in cm): The mean 3D metric error over all visible tracked points, with units converted from meters to centimeters.

$$ATE^{3D} = \left(\frac{\sum_{i=1}^{N} \sum_{v=1}^{V} m_{i,v} \cdot e_{i,v}^{3D}}{\sum_{i=1}^{N} \sum_{v=1}^{V} m_{i,v}}\right) \times 100 \quad (7)$$

 Accuracy (Acc@k cm): The percentage of visible points for which the 3D metric error is less than a threshold of k centimeters.

$$\text{Acc@k cm} = \frac{\sum_{i=1}^{N} \sum_{v=1}^{V} m_{i,v} \cdot \mathbb{I}(e_{i,v}^{3D} < k/100)}{\sum_{i=1}^{N} \sum_{v=1}^{V} m_{i,v}} \times 100\% \tag{8}$$

A.2. 3D Reconstruction

Finetune Setting. To ensure a fair and controlled comparison, we designed our experimental setup to specifically isolate the contribution of the feature encoder, as detailed in Tab. 7. We present more qualitative examples of reconstructed pointmaps in Fig. 12.

CroCo as backbone. Due to space constraints in the main manuscript, we focused primarily on comparisons with standard frame-wise backbones. To provide a deeper analysis of multi-view capabilities, we present additional comparisons with CroCo[46] in this section. CroCo is a representative method that learns cross-view consistency through pairwise masked image modeling. When utilizing CroCo[46] as a feature backbone, we explore two distinct strategies to extract latent representations from multiview inputs. The first setting is to treat CroCo solely as a feature extractor by utilizing only its encoder. Given a sequence of multi-view images, we reshape the batch to process each frame independently. Each image is passed through the CroCo encoder, and the output from the final encoder block is extracted as the latent representation. This approach aligns with standard frame-wise backbones like DINO[6], offering efficiency but lacking explicit cross-view interaction during feature extraction. The other strategy is to leverage its cross-view completion capability, where we employ a reference-based pairwise strategy. We select the first view in the sequence as the reference source. For every target view in the batch (including the first view), we construct a source-target pair and pass them through the full encoder-decoder pipeline. Specifically, both the reference and target images are encoded, and their features are then fed into the decoder, where cross-attention mechanisms allow the reference view to refine the target view's representation. We extract the output from the decoder blocks as the final, geometrically enriched features for the target view. While this method introduces cross-view context, it incurs a higher computational cost due to the pairwise processing of N views against a fixed reference. It is worth noting that the CroCo architecture consists of a ViT-Large encoder coupled with a ViT-Base decoder, resulting in a higher total parameter count compared to other baselines. This difference introduces a disparity in model capacity, theoretically biasing the comparison in favor of CroCo. Despite this unfair advantage in model capacity favoring CroCo, our method still achieves superior performance, highlighting the efficiency

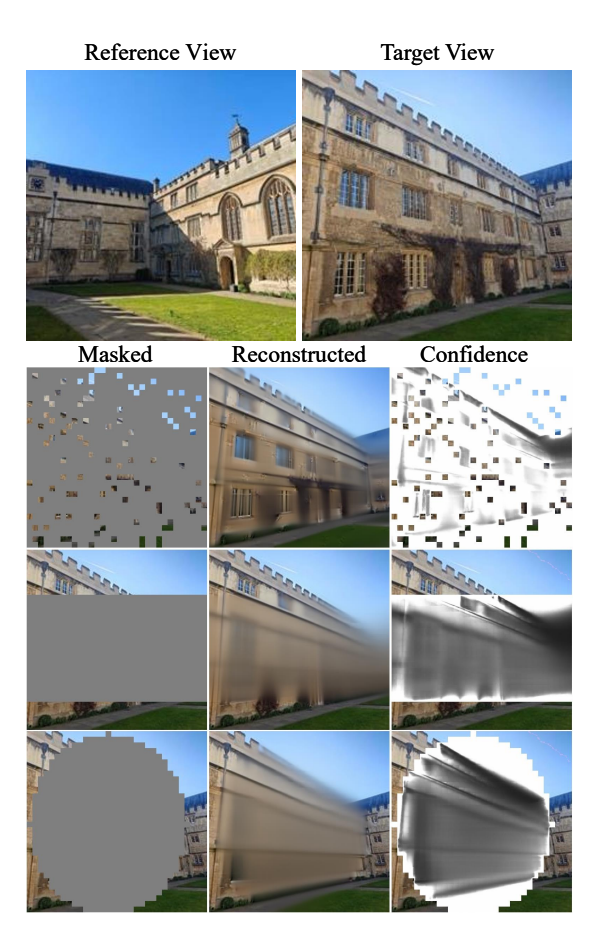


Figure 8. Reconstruction fails when there is no overlap between the reference view and the view to be reconstructed. Source images are from [40].

of our proposed approach, as shown in Tabs. 11 and 12.

A.3. Ablation Studies

Pretraining or Architecture. As shown in Fig. 7, using Muskie pretrained weights as a starting point leads to accelerated convergence speeds and superior training stability compared to random initialization, characterized by reduced loss variance and smoother optimization trajectories.

A.4. Pre-training

More results In this section, we further present additional cases where Muskie reconstructs complete images from masked multi-view inputs, as shown in Fig. 14. These examples were not used for training.

Non-overlapping Case When the input view pair contains no overlapping regions, Muskie's multi-view capability effectively degenerates into single-view masked image modeling. As shown in Fig. 8, with randomly scattered masks, the network can still exploit the remaining sparse visible

Method				Pixel Space	e (px)			3D Space (cm)					
Wedned	ATE _{2D} ↓	Acc@1px↑	Acc@2px↑	Acc@5px↑	Acc@10px↑	Acc@25px↑	Acc@50px↑	ATE _{3D} ↓	Acc@1cm↑	Acc@2cm↑	Acc@5cm↑	Acc@10cm↑	
DINOv2-B[23]	56.46	13.01	13.53	16.66	25.55	50.15	68.68	4.43	53.72	68.98	83.33	88.34	
DINOv2-L[23]	53.31	13.02	13.56	16.94	26.29	51.37	69.87	4.24	54.72	69.97	84.23	88.86	
DINOv3-B[32]	42.95	13.07	13.59	17.12	27.25	54.65	74.12	3.92	57.74	73.55	86.44	89.53	
DINOv3-L[32]	41.15	13.02	13.53	17.23	27.95	<u>57.11</u>	<u>76.14</u>	3.76	60.15	74.89	87.11	90.00	
SAM[19]	69.54	12.98	13.32	15.68	22.28	41.36	58.16	4.56	46.65	62.58	81.66	88.73	
MAE[14]	81.24	12.91	13.10	14.63	19.11	33.01	48.51	5.25	37.75	54.73	78.19	86.24	
DIFT[35]	60.44	13.01	13.56	16.97	26.46	49.55	63.75	4.93	51.00	64.36	81.21	86.83	
SigLIP[53]	111.66	12.86	12.94	13.66	15.71	24.21	37.64	7.79	28.37	43.46	68.41	79.35	
CLIP[24]	189.22	12.85	12.87	12.97	13.35	15.30	19.65	13.86	17.22	23.84	41.10	55.03	
CroCo[46]	56.79	13.15	14.07	19.77	32.58	54.77	69.74	4.42	58.13	72.15	84.66	87.39	
Muskie-B	42.54	13.15	14.03	19.48	31.95	56.17	73.86	2.93	60.92	75.90	89.17	93.30	
Muskie-L	29.42	13.28	14.53	22.29	39.21	68.69	83.98	2.38	71.03	82.74	91.87	94.32	

Table 9. Quantitative results for zero-shot point tracking on the NAVI [16] dataset across 8 views. We compare our Muskie models against a comprehensive set of foundational models. Best results are in **bold**, and underlined results indicate the second best.

Method				Pixel Space	e (px)			3D Space (cm)					
Wedned	ATE _{2D} ↓	Acc@1px↑	Acc@2px↑	Acc@5px↑	Acc@10px↑	Acc@25px↑	Acc@50px↑	ATE _{3D} ↓	Acc@1cm↑	Acc@2cm↑	Acc@5cm↑	Acc@10cm↑	
DINOv2-B[23]	72.41	20.76	21.19	23.17	29.32	45.87	60.31	49.88	24.57	27.31	35.00	45.71	
DINOv2-L[23]	72.11	20.85	21.26	23.42	29.22	44.16	59.17	49.09	24.55	27.13	34.29	44.64	
DINOv3-B[32]	64.07	20.83	21.17	24.41	32.08	53.74	66.77	46.15	25.08	28.98	40.22	51.09	
DINOv3-L[32]	55.78	20.85	21.26	24.66	33.54	56.06	70.32	42.58	25.27	29.49	41.69	52.87	
SAM[19]	76.12	20.77	21.01	23.80	31.16	47.85	60.31	49.85	24.01	27.34	36.56	46.05	
MAE[14]	104.94	20.70	20.85	22.07	25.18	33.48	44.10	62.70	22.81	24.01	28.51	34.89	
DIFT[35]	69.82	20.88	21.55	26.44	39.21	59.86	68.15	50.56	25.76	31.65	44.28	54.62	
SigLIP[53]	142.96	20.68	20.74	21.04	21.78	26.16	34.02	81.44	22.72	23.04	24.88	28.75	
CLIP[24]	203.18	20.67	20.67	20.83	21.04	22.21	25.09	102.45	22.30	22.47	22.95	24.34	
CroCo[46]	25.92	21.19	23.08	34.20	55.93	80.09	89.27	29.84	28.19	38.16	58.02	72.08	
Muskie-B	33.77	21.24	22.77	31.41	47.67	68.37	81.60	31.67	27.18	35.03	51.14	63.92	
Muskie-L	24.68	21.33	23.15	33.83	<u>52.96</u>	<u>76.49</u>	<u>87.90</u>	27.82	28.44	<u>37.52</u>	<u>56.60</u>	<u>70.84</u>	

Table 10. Quantitative results for zero-shot point tracking on the ScanNet[8] dataset across 8 views. We compare our Muskie models against a comprehensive set of foundational models. Best results are in **bold**, and underlined results indicate the second best.

Method	N	RGBD[4	4]	7:	7Scenes[31]				
1,10111011	Acc	Comp	$ \mathcal{L}_1 $	Acc	Comp	$ \mathcal{L}_1 $			
CroCo (encoder)	0.0647	0.1127	0.1179	0.0429	0.0526	0.0864			
CroCo (decoder)	0.0541	0.0889	0.0823	0.0311	0.0321	0.0491			
Muskie-B	0.0585	0.0896	0.0897	0.0391	0.0405	0.0508			
Muskie-L	0.0460	0.0765	0.0667	0.0249	0.0283	0.0346			

Table 11. Performance comparison on pointmap across NRGBD [4] and 7Scenes[31] datasets.

Method	1	NRGBD[4]	7Scenes[31]				
1,1011101	$\overline{\text{AUC}_5}$	AUC_{15}	AUC ₃₀	$\overline{AUC_5}$	AUC_{15}	AUC ₃₀		
CroCo (encoder)	0.63	7.12	16.92	0.23	2.86	9.98		
CroCo (decoder)	7.03	28.56	45.45	2.96	16.34	32.60		
Muskie-B	3.69	25.04	45.43	1.41	13.81	31.23		
Muskie-L	19.46	50.96	67.45	6.10	26.93	47.35		

Table 12. Camera pose estimation performance (AUC) comparison on NRGBD [4] and 7Scenes[31] datasets.

patches to reconstruct the target, exhibiting behavior similar to MAE[14]. In contrast, when large aggregated masks are

applied, most intra-view structural cues are removed. Without cross-view information to compensate for the missing content, the model produces blurred reconstructions, and the low confidence indicates the absence of usable multiview cues.

A.5. Qualitative Feature Analysis

In this section, we qualitatively analyze Muskie's dense feature representations. To this end, we project the high-dimensional feature space into three dimensions using principal component analysis (PCA), and visualize the resulting 3D embeddings by mapping them to RGB. All experiments use Muskie-L as the feature extractor. Fig. 9 shows feature maps from layers 4, 8, 12, 16, 20, and 24. Notably, the 20th layer yields the most visually interpretable representation. In contrast, the final layer exhibits degraded visual structure due to the pixel-level reconstruction objective: its supervision signal is low-dimensional and highly ambiguous, which corrupts the high-level semantics in the features. We use the 20th layer for all subsequent visualizations.

Fig. 10 compares Muskie's single-view feature maps with those produced by DINOv3. While DINOv3 features

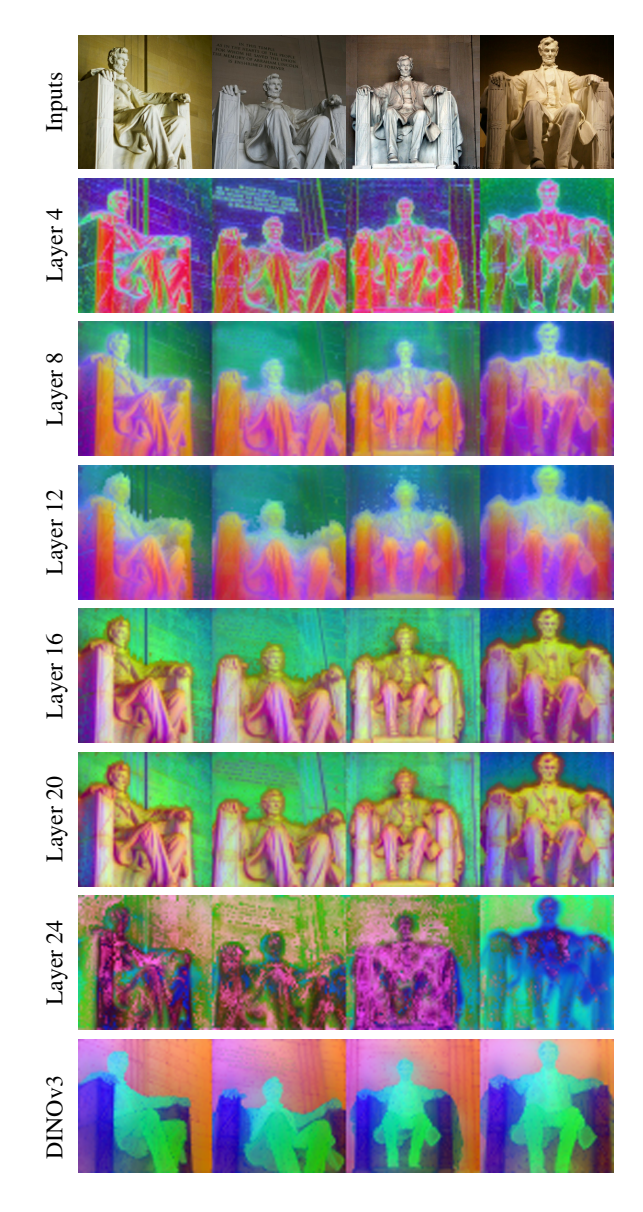


Figure 9. PCA feature visualization across layers of Muskie-L. DINOv3 features are plotted on the last line.

display strong semantic consistency, they lose fine-grained structural details. This property benefits high-level tasks that rely on semantic abstraction but is less suitable for low-level reconstruction tasks that depend on precise feature matching. In contrast, Muskie's features preserve detailed geometry and object boundaries and exhibit strong cross-view consistency, making them substantially more suitable for reconstruction-oriented downstream applications. Additional multi-view visualizations are provided in Fig. 11, where corresponding points across views show consistent features that are largely invariant to illumination and view-point changes.

A.6. Computational complexity

As shown in Tab. 8, we evaluate the inference runtime of our proposed Muskie backbone against the state-of-the-art frame-wise baseline, DINOv3. Measurements are conducted using a single NVIDIA A100 GPU with bfloat16 precision. Input images have a resolution of 224×224 . Both models leverage PyTorch's optimized scaled_dot_product_attention operator for fair comparison. While DINOv3 exhibits linear scaling $(\mathcal{O}(N))$ due to independent frame processing, Muskie employs global attention for half layers, theoretically leading to quadratic scaling $(\mathcal{O}(N^2))$. This sacrifice in inference speed is a necessary trade-off to move beyond the limitations of frame-wise procesing.

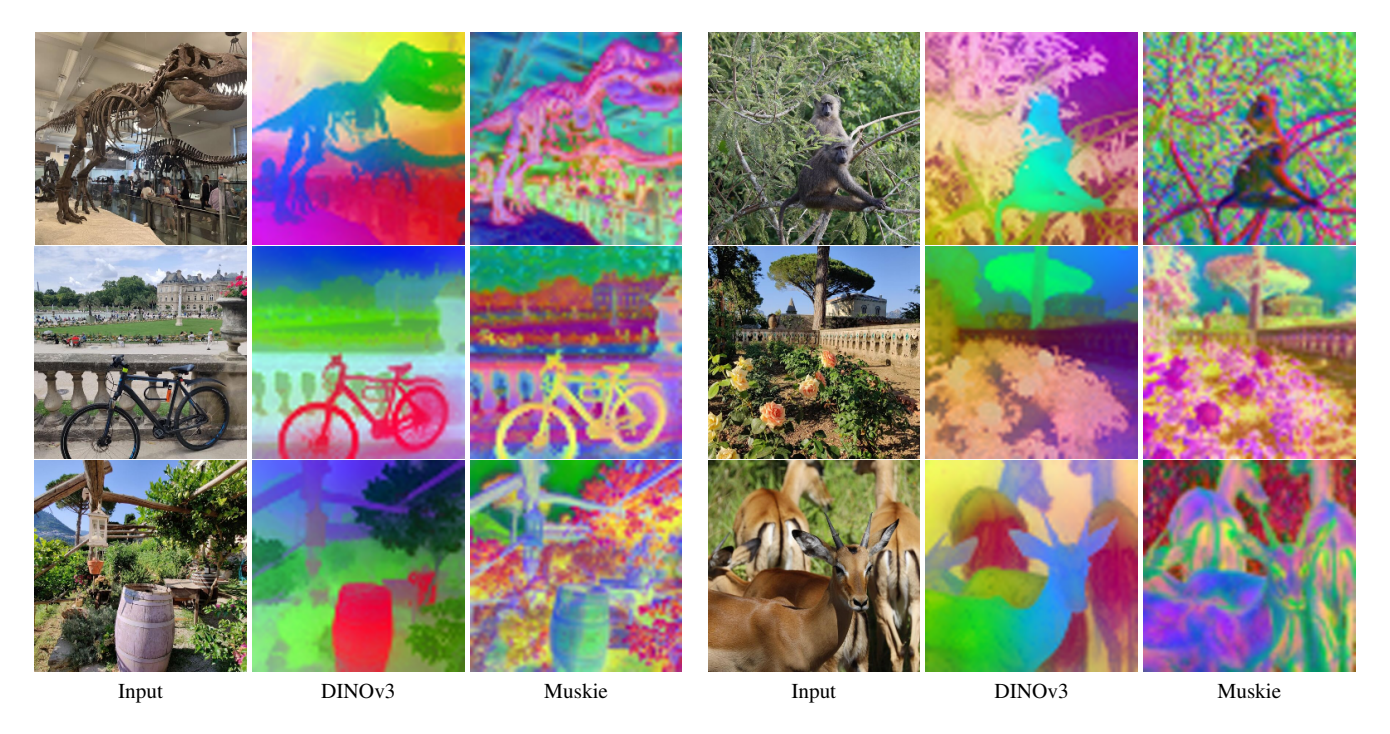


Figure 10. PCA feature visualization for single-view images, compared to DINOv3.

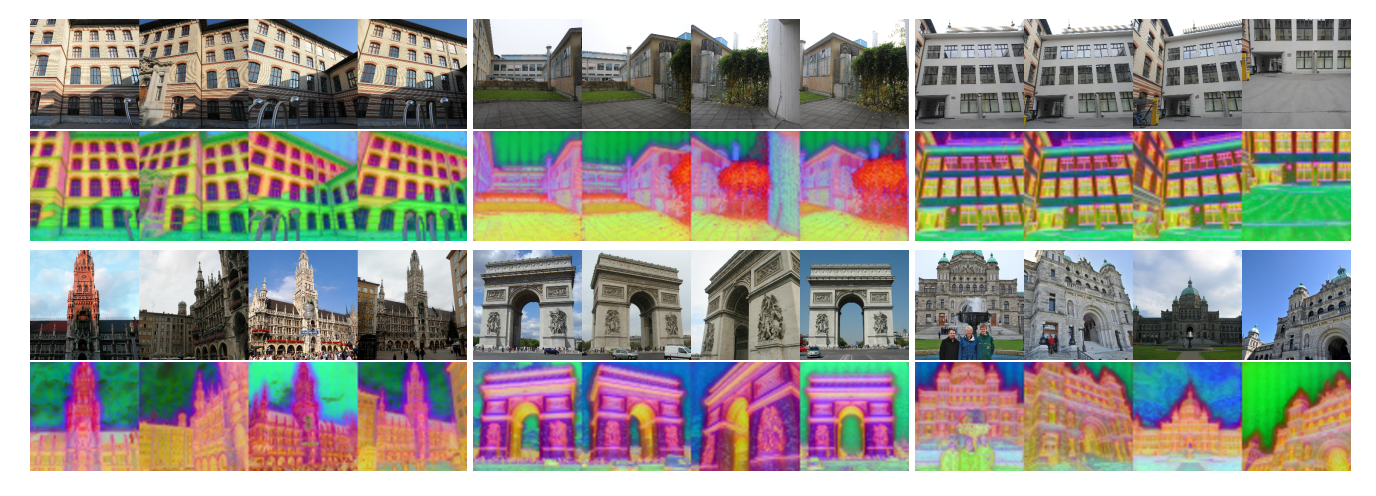


Figure 11. PCA feature visualization for multi-view images.

References

- [1] Karim Abou Zeid, Kadir Yilmaz, Daan de Geus, Alexander Hermans, David Adrian, Timm Linder, and Bastian Leibe. DINO in the room: Leveraging 2D foundation models for 3D segmentation. In 2026 International Conference on 3D Vision (3DV), 2026. 2
- [2] Honggyu An, Jin Hyeon Kim, Seonghoon Park, Jaewoo Jung, Jisang Han, Sunghwan Hong, and Seungryong Kim. Cross-view completion models are zero-shot correspondence estimators. In *Proceedings of the Computer Vision and Pattern Recognition Conference*, pages 1103–1115, 2025. 9
- [3] Pattaramanee Arsomngern, Sarana Nutanong, and Supasorn

- Suwajanakorn. Learning geometric-aware properties in 2d representation using lightweight cad models, or zero real 3d pairs. 2023 IEEE/CVF Conference on Computer Vision and Pattern Recognition (CVPR), pages 21371–21381, 2023. 2
- [4] Dejan Azinović, Ricardo Martin-Brualla, Dan B Goldman, Matthias Nießner, and Justus Thies. Neural rgb-d surface reconstruction. In *Proceedings of the IEEE/CVF Conference* on Computer Vision and Pattern Recognition (CVPR), pages 6290–6301, 2022. 5, 6, 7, 8, 12, 15, 16, 19
- [5] Gilad Baruch, Zhuoyuan Chen, Afshin Dehghan, Tal Dimry, Yuri Feigin, Peter Fu, Thomas Gebauer, Brandon Joffe, Daniel Kurz, Arik Schwartz, and Elad Shulman. ARKitscenes - a diverse real-world dataset for 3d indoor scene



Figure 12. Qualitative comparison of predicted pointmaps for NRGBD[4] and 7Scenes[31].

- understanding using mobile RGB-d data. In *Thirty-fifth Conference on Neural Information Processing Systems Datasets and Benchmarks Track (Round 1)*, 2021. 4, 7
- [6] Mathilde Caron, Hugo Touvron, Ishan Misra, Hervé Jégou, Julien Mairal, Piotr Bojanowski, and Armand Joulin. Emerging properties in self-supervised vision transformers. In *Proceedings of the IEEE/CVF international conference on com-*
- puter vision, pages 9650-9660, 2021. 2, 11
- [7] Ting Chen, Simon Kornblith, Mohammad Norouzi, and Geoffrey Hinton. A simple framework for contrastive learning of visual representations. In *International conference on machine learning*, pages 1597–1607. PMLR, 2020. 2
- [8] Angela Dai, Angel X. Chang, Manolis Savva, Maciej Halber, Thomas Funkhouser, and Matthias Nießner. Scannet:

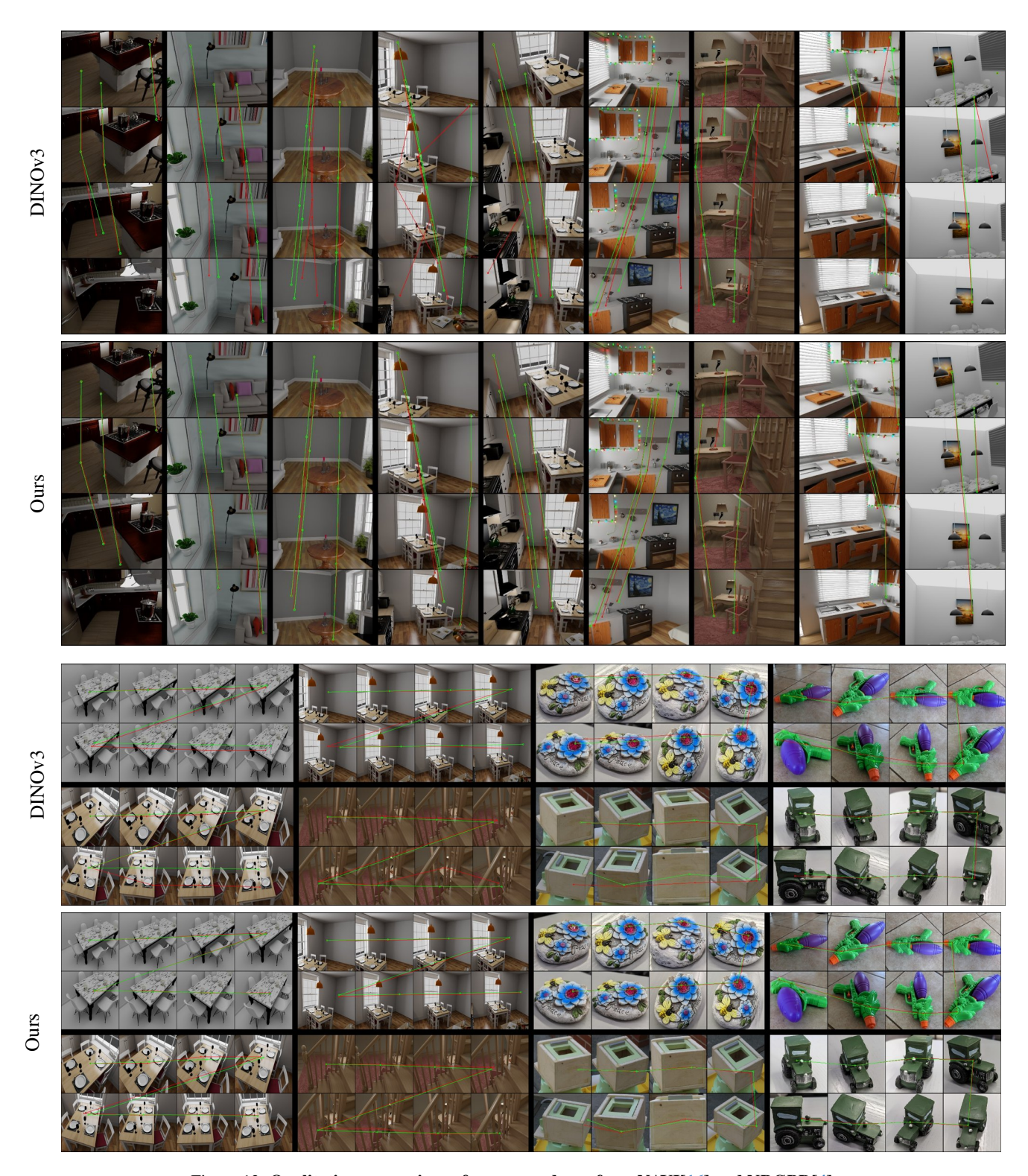


Figure 13. Qualitative comparison of correspondence from NAVI[16] and NRGBD[4].

Richly-annotated 3d reconstructions of indoor scenes. In *Proc. Computer Vision and Pattern Recognition (CVPR), IEEE*, 2017. 5, 6, 7, 12

[9] Kai Deng, Zexin Ti, Jiawei Xu, Jian Yang, and Jin Xie. Vggtlong: Chunk it, loop it, align it – pushing vggt's limits on kilometer-scale long rgb sequences, 2025. 1, 2

- [10] Jacob Devlin, Ming-Wei Chang, Kenton Lee, and Kristina Toutanova. BERT: pre-training of deep bidirectional transformers for language understanding. *CoRR*, abs/1810.04805, 2018. 2
- [11] Mohamed El Banani, Amit Raj, Kevis-Kokitsi Maninis, Abhishek Kar, Yuanzhen Li, Michael Rubinstein, Deqing Sun, Leonidas Guibas, Justin Johnson, and Varun Jampani. Probing the 3d awareness of visual foundation models. In *Proceedings of the IEEE/CVF Conference on Computer Vision and Pattern Recognition*, pages 21795–21806, 2024. 1, 5
- [12] Jean-Bastien Grill, Florian Strub, Florent Altché, Corentin Tallec, Pierre H. Richemond, Elena Buchatskaya, Carl Doersch, Bernardo Ávila Pires, Zhaohan Daniel Guo, Mohammad Gheshlaghi Azar, Bilal Piot, Koray Kavukcuoglu, Rémi Munos, and Michal Valko. Bootstrap your own latent: A new approach to self-supervised learning. In *Proc. NeurIPS*, 2020. 2
- [13] Kaiming He, Haoqi Fan, Yuxin Wu, Saining Xie, and Ross B. Girshick. Momentum contrast for unsupervised visual representation learning. *arXiv.cs*, abs/1911.05722, 2019. 2
- [14] Kaiming He, Xinlei Chen, Saining Xie, Yanghao Li, Piotr Dollár, and Ross B. Girshick. Masked autoencoders are scalable vision learners. In *Proc. CVPR*, 2021. 2, 3, 4, 6, 7, 12
- [15] Ji Hou, Saining Xie, Benjamin Graham, Angela Dai, and Matthias Nießner. Pri3d: Can 3d priors help 2d representation learning? In 2021 IEEE/CVF International Conference on Computer Vision (ICCV), pages 5673–5682, 2021. 1, 2
- [16] Varun Jampani, Kevis-Kokitsi Maninis, Andreas Engelhardt, Karen Truong, Arjun Karpur, Kyle Sargent, Stefan Popov, Andre Araujo, Ricardo Martin-Brualla, Kaushal Patel, Daniel Vlasic, Vittorio Ferrari, Ameesh Makadia, Ce Liu, Yuanzhen Li, and Howard Zhou. NAVI: Categoryagnostic image collections with high-quality 3d shape and pose annotations. In *NeurIPS*, 2023. 5, 6, 7, 8, 12, 16
- [17] Nikhil Keetha, Norman Müller, Johannes Schönberger, Lorenzo Porzi, Yuchen Zhang, Tobias Fischer, Arno Knapitsch, Duncan Zauss, Ethan Weber, Nelson Antunes, Jonathon Luiten, Manuel Lopez-Antequera, Samuel Rota Bulò, Christian Richardt, Deva Ramanan, Sebastian Scherer, and Peter Kontschieder. MapAnything: Universal feedforward metric 3D reconstruction. In arXiv:2509.13414, 2025. 1, 2
- [18] Diederik P Kingma and Jimmy Ba. Adam: A method for stochastic optimization. arXiv preprint arXiv:1412.6980, 2014. 5
- [19] Alexander Kirillov, Eric Mintun, Nikhila Ravi, Hanzi Mao, Chloe Rolland, Laura Gustafson, Tete Xiao, Spencer Whitehead, Alexander C. Berg, Wan-Yen Lo, Piotr Dollár, and Ross Girshick. Segment anything. arXiv:2304.02643, 2023. 6, 12
- [20] Feng Li, Hao Zhang, Huaizhe xu, Shilong Liu, Lei Zhang, Lionel M. Ni, and Heung-Yeung Shum. Mask dino: Towards a unified transformer-based framework for object detection and segmentation, 2022. 2
- [21] Zhengqi Li and Noah Snavely. Megadepth: Learning singleview depth prediction from internet photos. In *Proceed*-

- ings of the IEEE conference on computer vision and pattern recognition, pages 2041–2050, 2018. 4
- [22] Lu Ling, Yichen Sheng, Zhi Tu, Wentian Zhao, Cheng Xin, Kun Wan, Lantao Yu, Qianyu Guo, Zixun Yu, Yawen Lu, et al. Dl3dv-10k: A large-scale scene dataset for deep learning-based 3d vision. In Proceedings of the IEEE/CVF Conference on Computer Vision and Pattern Recognition, pages 22160–22169, 2024. 4
- [23] Maxime Oquab, Timothée Darcet, Théo Moutakanni, Huy V. Vo, Marc Szafraniec, Vasil Khalidov, Pierre Fernandez, Daniel HAZIZA, Francisco Massa, Alaaeldin El-Nouby, Mido Assran, Nicolas Ballas, Wojciech Galuba, Russell Howes, Po-Yao Huang, Shang-Wen Li, Ishan Misra, Michael Rabbat, Vasu Sharma, Gabriel Synnaeve, Hu Xu, Herve Jegou, Julien Mairal, Patrick Labatut, Armand Joulin, and Piotr Bojanowski. DINOv2: Learning robust visual features without supervision. Transactions on Machine Learning Research, 2024. 1, 2, 6, 7, 10, 12
- [24] Alec Radford, Jong Wook Kim, Chris Hallacy, Aditya Ramesh, Gabriel Goh, Sandhini Agarwal, Girish Sastry, Amanda Askell, Pamela Mishkin, Jack Clark, Gretchen Krueger, and Ilya Sutskever. Learning transferable visual models from natural language supervision. In *Proc. ICML*, pages 8748–8763, 2021. 6, 12
- [25] Jeremy Reizenstein, Roman Shapovalov, Philipp Henzler, Luca Sbordone, Patrick Labatut, and David Novotny. Common Objects in 3D: Large-scale learning and evaluation of real-life 3D category reconstruction. In *Proc. ICCV*, 2021. 4
- [26] Mike Roberts, Jason Ramapuram, Anurag Ranjan, Atulit Kumar, Miguel Angel Bautista, Nathan Paczan, Russ Webb, and Joshua M. Susskind. Hypersim: A photorealistic synthetic dataset for holistic indoor scene understanding. In *International Conference on Computer Vision (ICCV)* 2021, 2021. 4
- [27] Paul-Edouard Sarlin, Daniel DeTone, Tomasz Malisiewicz, and Andrew Rabinovich. SuperGlue: learning feature matching with graph neural networks. In *Proc. CVPR*, 2020.
- [28] Johannes Lutz Schönberger and Jan-Michael Frahm. Structure-from-motion revisited. In Proc. CVPR, 2016.
- [29] Johannes Lutz Schönberger, Enliang Zheng, Marc Pollefeys, and Jan-Michael Frahm. Pixelwise view selection for unstructured multi-view stereo. In *European Conference on Computer Vision (ECCV)*, 2016. 1
- [30] Thomas Schops, Johannes L Schonberger, Silvano Galliani, Torsten Sattler, Konrad Schindler, Marc Pollefeys, and Andreas Geiger. A multi-view stereo benchmark with high-resolution images and multi-camera videos. In *Proceedings of the IEEE conference on computer vision and pattern recognition*, pages 3260–3269, 2017. 4, 19
- [31] Jamie Shotton, Ben Glocker, Christopher Zach, Shahram Izadi, Antonio Criminisi, and Andrew Fitzgibbon. Scene coordinate regression forests for camera relocalization in rgb-d images. In 2013 IEEE Conference on Computer Vision and Pattern Recognition, pages 2930–2937, 2013. 4, 5, 6, 7, 8, 12, 15, 19
- [32] Oriane Siméoni, Huy V Vo, Maximilian Seitzer, Federico Baldassarre, Maxime Oquab, Cijo Jose, Vasil Khalidov,

- Marc Szafraniec, Seungeun Yi, Michaël Ramamonjisoa, et al. Dinov3. *arXiv preprint arXiv:2508.10104*, 2025. 1, 2, 6, 7, 12
- [33] Jianlin Su, Murtadha Ahmed, Yu Lu, Shengfeng Pan, Wen Bo, and Yunfeng Liu. Roformer: Enhanced transformer with rotary position embedding. *Neurocomputing*, 568:127063, 2024. 4
- [34] Pei Sun, Henrik Kretzschmar, Xerxes Dotiwalla, Aurélien Chouard, Vijaysai Patnaik, Paul Tsui, James Guo, Yin Zhou, Yuning Chai, Benjamin Caine, Vijay Vasudevan, Wei Han, Jiquan Ngiam, Hang Zhao, Aleksei Timofeev, Scott Ettinger, Maxim Krivokon, Amy Gao, Aditya Joshi, Yu Zhang, Jonathon Shlens, Zhifeng Chen, and Dragomir Anguelov. Scalability in perception for autonomous driving: Waymo open dataset. In 2020 IEEE/CVF Conference on Computer Vision and Pattern Recognition (CVPR), pages 2443–2451, 2020. 4
- [35] Luming Tang, Menglin Jia, Qianqian Wang, Cheng Perng Phoo, and Bharath Hariharan. Emergent correspondence from image diffusion. In *Thirty-seventh Conference on Neural Information Processing Systems*, 2023. 6, 12
- [36] Zhan Tong, Yibing Song, Jue Wang, and Limin Wang. VideoMAE: Masked autoencoders are data-efficient learners for self-supervised video pre-training. In Advances in Neural Information Processing Systems, 2022. 2
- [37] Bill Triggs. Camera pose and calibration from 4 or 5 known 3D points. In *Proc. ICCV*, 1999. 1
- [38] Bill Triggs, Philip F. McLauchlan, Richard I. Hartley, and Andrew W. Fitzgibbon. Bundle adjustment - A modern synthesis. In *Proc. ICCV Workshop*, 2000. 1
- [39] Shinji Umeyama. Least-squares estimation of transformation parameters between two point patterns. *IEEE Transactions on Pattern Analysis & Machine Intelligence*, 13(04): 376–380, 1991. 7
- [40] Jianyuan Wang, Minghao Chen, Nikita Karaev, Andrea Vedaldi, Christian Rupprecht, and David Novotny. Vggt: Visual geometry grounded transformer. In *Proceedings of the Computer Vision and Pattern Recognition Conference*, pages 5294–5306, 2025. 1, 2, 3, 4, 7, 11
- [41] Qianqian Wang, Xiaowei Zhou, Bharath Hariharan, and Noah Snavely. Learning feature descriptors using camera pose supervision. In *Proc. European Conference on Computer Vision (ECCV)*, 2020. 2
- [42] Ruicheng Wang, Sicheng Xu, Cassie Dai, Jianfeng Xiang, Yu Deng, Xin Tong, and Jiaolong Yang. MoGe: unlocking accurate monocular geometry estimation for opendomain images with optimal training supervision. *arXiv*, 2410.19115, 2024. 2
- [43] Shuzhe Wang, Vincent Leroy, Yohann Cabon, Boris Chidlovskii, and Jerome Revaud. DUSt3R: Geometric 3D vision made easy. In *Proc. CVPR*, 2024. 2
- [44] Yifan Wang, Jianjun Zhou, Haoyi Zhu, Wenzheng Chang, Yang Zhou, Zizun Li, Junyi Chen, Jiangmiao Pang, Chunhua Shen, and Tong He. π^3 : Scalable permutation-equivariant visual geometry learning. *arXiv preprint arXiv:2507.13347*, 2025. 1, 2, 6, 7, 10

- [45] Philippe Weinzaepfel, Vincent Leroy, Thomas Lucas, Romain Brégier, Yohann Cabon, Vaibhav Arora, Leonid Antsfeld, Boris Chidlovskii, Gabriela Csurka, and Jérôme Revaud. Croco: Self-supervised pre-training for 3d vision tasks by cross-view completion. Advances in Neural Information Processing Systems, 35:3502–3516, 2022. 2, 3
- [46] Philippe Weinzaepfel, Thomas Lucas, Vincent Leroy, Yohann Cabon, Vaibhav Arora, Romain Brégier, Gabriela Csurka, Leonid Antsfeld, Boris Chidlovskii, and Jérôme Revaud. Croco v2: Improved cross-view completion pretraining for stereo matching and optical flow. In Proceedings of the IEEE/CVF International Conference on Computer Vision, pages 17969–17980, 2023. 2, 3, 6, 11, 12
- [47] Zhenda Xie, Zheng Zhang, Yue Cao, Yutong Lin, Jianmin Bao, Zhuliang Yao, Qi Dai, and Han Hu. Simmin: A simple framework for masked image modeling. In *Proceedings of the IEEE/CVF conference on computer vision and pattern recognition*, pages 9653–9663, 2022. 2
- [48] Jianing Yang, Alexander Sax, Kevin J Liang, Mikael Henaff, Hao Tang, Ang Cao, Joyce Chai, Franziska Meier, and Matt Feiszli. Fast3r: Towards 3d reconstruction of 1000+ images in one forward pass. arXiv preprint arXiv:2501.13928, 2025.
- [49] Lihe Yang, Bingyi Kang, Zilong Huang, Xiaogang Xu, Jiashi Feng, and Hengshuang Zhao. Depth anything: Unleashing the power of large-scale unlabeled data. In CVPR, 2024. 2
- [50] Lihe Yang, Bingyi Kang, Zilong Huang, Zhen Zhao, Xiao-gang Xu, Jiashi Feng, and Hengshuang Zhao. Depth anything v2. arXiv:2406.09414, 2024. 2
- [51] Yao Yao, Zixin Luo, Shiwei Li, Jingyang Zhang, Yufan Ren, Lei Zhou, Tian Fang, and Long Quan. Blendedmys: A largescale dataset for generalized multi-view stereo networks. In Proceedings of the IEEE/CVF conference on computer vision and pattern recognition, pages 1790–1799, 2020. 4, 7
- [52] Chandan Yeshwanth, Yueh-Cheng Liu, Matthias Nießner, and Angela Dai. Scannet++: A high-fidelity dataset of 3d indoor scenes. In *Proceedings of the International Conference on Computer Vision (ICCV)*, 2023. 4, 7
- [53] Xiaohua Zhai, Basil Mustafa, Alexander Kolesnikov, and Lucas Beyer. Sigmoid loss for language image pre-training. 2023 IEEE/CVF International Conference on Computer Vision (ICCV), pages 11941–11952, 2023. 6, 12
- [54] Tinghui Zhou, Richard Tucker, John Flynn, Graham Fyffe, and Noah Snavely. Stereo magnification: Learning view synthesis using multiplane images. arXiv preprint arXiv:1805.09817, 2018. 4
- [55] Dong Zhuo, Wenzhao Zheng, Jiahe Guo, Yuqi Wu, Jie Zhou, and Jiwen Lu. Streaming 4d visual geometry transformer. arXiv preprint arXiv:2507.11539, 2025. 1, 2



Figure 14. Additional examples of reconstruction from masked multi-view images[4, 30, 31].